# Controlled Doping of Electrocatalysts through Engineering Impurities

*Se-Ho Kim,\* Su-Hyun Yoo, Sangyong Shin, Ayman A. El-Zoka, Olga Kasian, Joohyun Lim, Jiwon Jeong, Christina Scheu, Jörg Neugebauer, Hyunjoo Lee, Mira Todorova, and Baptiste Gault\**

Fuel cells recombine water from $H_2$ and $O_2$ thereby can power, for example, cars or houses with no direct carbon emission. In anion-exchange membrane fuel cells (AEMFCs), to reach high power densities, operating at high pH is an alternative to using large volumes of noble metals catalysts at the cathode, where the oxygen-reduction reaction occurs. However, the sluggish kinetics of the hydrogen-oxidation reaction (HOR) hinders upscaling despite promising catalysts. Here, the authors observe an unexpected ingress of B into Pd nanocatalysts synthesized by wet-chemistry, gaining control over this B-doping, and report on its influence on the HOR activity in alkaline conditions. They rationalize their findings using ab initio calculations of both H- and OH-adsorption on B-doped Pd. Using this "impurity engineering" approach, they thus design Pt-free catalysts as required in electrochemical energy conversion devices, for example, next generations of AEMFCs, that satisfy the economic and environmental constraints, that is, reasonable operating costs and long-term stability, to enable the "hydrogen economy."

S.-H. Kim, S.-H. Yoo, A. A. El-Zoka, O. Kasian, J. Lim, J. Jeong, C. Scheu, J. Neugebauer, M. Todorova, B. Gault
Max-Planck Institut für Eisenforschung GmbH
Max-Planck-Straße 1, 40237 Düsseldorf, Germany
E-mail: s.kim@mpie.de; b.gault@mpie.de

S. Shin, H. Lee
Department of Chemical and Biomolecular Engineering
Korea Advanced Institute of Science and Technology
Daejeon 34141, Republic of Korea

O. Kasian
Helmholtz-Zentrum Berlin GmbH
Helmholtz Institut Erlangen-Nürnberg
14109 Berlin, Germany

J. Lim
Department of Chemistry
Kangwon National University
Chuncheon 24342, Republic of Korea

B. Gault
Department of Materials
Royal School of Mines
Imperial College
London SW7 2AZ, UK

## 1. Introduction

Green hydrogen is produced by electrolyzers powered by solar,[1,2] wind,[3] geothermal,[4] or tidal[5] renewable energy. Whenever needed, $H_2$ is supplied to fuel cells to generate electricity with an efficiency reaching 93.5%[6] and no direct carbon emissions. However, to compete with fossil fuel-based power generation, these electrochemical energy conversion devices need new materials that are affordable and durable. In alkaline fuel cells,[7] non-noble metal-based electro-catalysts for the cathodic oxygen reduction reaction with activity and durability comparable or superior to the scarce Pt have been reported.[8,9] However, the kinetics of the anodic HOR in alkaline conditions is too slow, which is true also for Pt-group metal catalysts.[10] Pd nanocatalysts with oxophilic cerium oxides exhibited the highest recorded HOR specific exchange current (51.5 mA $mg^{-1}_{Pd}$)[11] in alkaline electrolytes. The high loads of precious metals required hinder upscaling the commercial development of efficient anion-exchange membrane fuel cells[12,13] and it motivates the search for new materials.

In our previous work, we have seen different unexpected impurities inside catalysts synthesized by wet chemistry, for example, Na in $TiO_2$ nanowires,[14] W in $MoS_2$ nanosheets,[15] cetrimonium ligand on multiple-twinned Pd nanoparticles,[16] C in Au–Fe nanoalloys.[17] Taking into account thermodynamics, these results are not completely surprising. The mixing entropy of system increases and the Gibbs free energy decreases when impurities are added to a pure substance. Therefore, trace amounts of elemental impurities from precursor chemicals are favorably integrated into the nanomaterial during fabrication. How this contamination from synthesis of electrochemical catalysts affects the materials' activity is however rarely examined and discussed.

We also recently reported that using sodium borohydride ($NaBH_4$) as reducing agent in room temperature synthesis of free-standing Pd nanocatalysts led to an ingress of impurities from the aqueous solution, that is, Na and K.[18] The absence of surfactant, used to avoid agglomeration, leads to the formation of a complex aggregated structure previously referred to as a metallic nano-aerogel (MNA).[19,20] Ever since its

discovery during World War II, NaBH$_4$ has been widely used in synthetic chemistry.[21] Its excellent reducing properties result in lower operation input, for example, no heating or additional organics are required to reduce metallic precursors. NaBH$_4$ has commonly been used to synthesize metal nanoparticles for catalytic,[22] antimicrobial,[23] electrochemical,[24] and optical[25] applications. However, the concentration of B impurities in the products is rarely considered,[26] and not systematically studied, yet the presence of B increases the lattice parameter[27] and could greatly modify the material's properties.

Here, we predict the stable integration of B within growing Pd-crystals and use theoretical guidelines to design a set of Pd-MNAs, with adjustable composition. We assess their performance toward the HOR in alkaline conditions and demonstrate the effect of the ingress of B from the solution into the material. Our impurity-doping approach could be generalized to help design in silico future catalysts with enhanced activity by estimating the adsorption properties of various elements and their influence on the H- and OH-binding energies.

## 2. Results and Discussion

First, we performed density-functional theory (DFT) calculations (see Experimental Section for computational details) to calculate the B binding energies on a Pd(111) surface. **Figure 1**a reports the respective energies for different high symmetry adsorption sites at and below the surface for increasing B coverage up to 1 monolayer (ML), where the number of adsorbates equals the number of substrate atoms in the first layer. Over this entire coverage range, the interstitial octahedral subsurface site (B$_{Octa}$) is the most favorable, and B should be predominantly in the subsurface rather than the surface region of Pd.

To prove this hypothesis, we mixed 0.4 M of NaBH$_4$ and 0.01 M of K$_2$PdCl$_4$, that is, a ratio of reductant to precursor of (R:P) 40, to synthesize a Pd-MNA referred to as Pd-B$_{40}$ based on the nomenclature introduced in ref. [18]. High-angle annular dark-field scanning- and high-resolution transmission electron microscopy (HAADF-STEM and HR-TEM) in Figure 1b show an average ligament thickness of ≈15 nm. The fast Fourier transform (FFT) pattern given as inset proves the face-centered cubic (FCC) structure of Pd. No particular elemental signal except Pd is obtained for the Pd-B$_{40}$ by X-ray photoelectron spectroscopy (XPS, see Figures S1–S3, Supporting Information). We then use atom probe tomography (APT) to evaluate the composition and elemental distribution in Pd-B$_{40}$ (see Experimental Section and the Supporting Information). Figure 1c shows the reconstructed 3D atom map. A set of iso-surfaces delineates regions containing at least 50 at% Pd (purple) and 75 at% Ni (yellow), highlighting the gel and the Ni-matrix that embed the nanocatalyst to facilitate specimen preparation.[28] The ligaments size is comparable to HAADF-STEM observations. A slice through the APT point cloud, Figure 1d, shows that B (in blue) is located inside Pd-B$_{40}$, not segregated to its surface, and the 1D composition profile, Figure 1e, confirms the ingress of over 2 at% B within the Pd nanocatalyst. A nearest-neighbor analysis indicates no B clustering tendency within the resolution limits of APT,[29,30] Figure S13, Supporting Information.
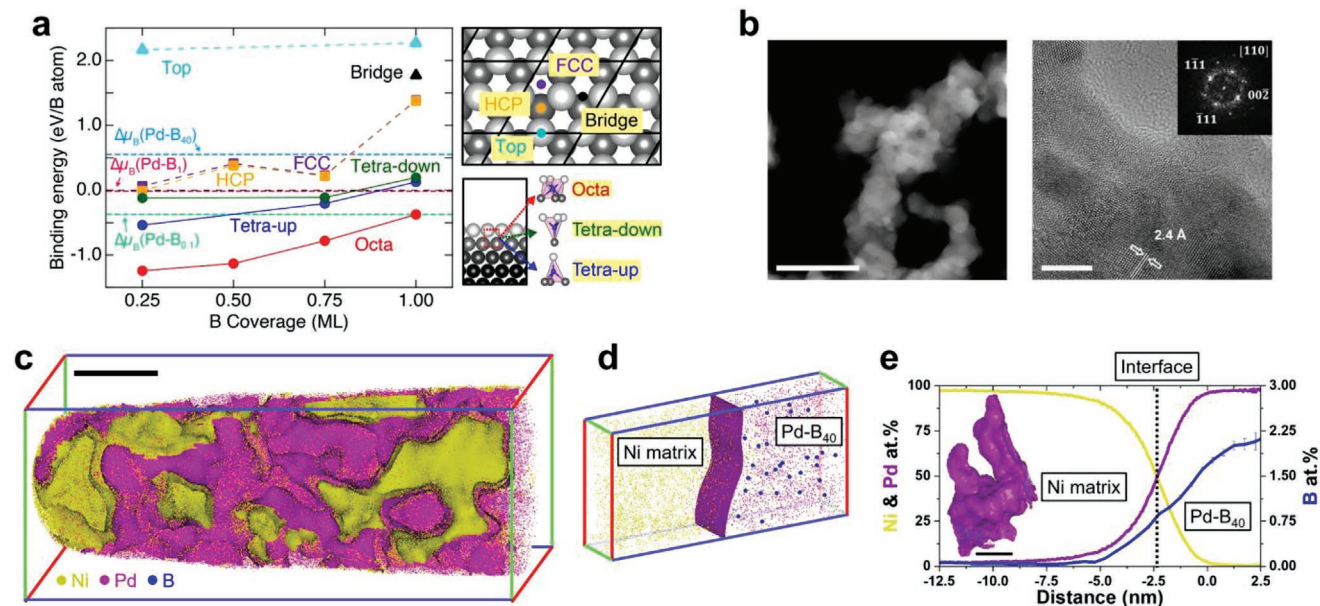


**Figure 1.** DFT calculation and high-resolution microscopy and microanalysis of B-incorporating Pd nanomaterials. a) Binding energies $E_b$ of B adsorbates at the Pd(111) surface and subsurface for several adsorbate coverages in the range from 0.25 to 1 ML. Each colored solid line corresponds to a different B binding site. Different chemical potentials of B$_x$ ($x$ gives the reductant to precursor ratio) of the considered synthesis conditions are shown as horizontal colored dashed lines. The possible binding sites at the surface are shown (top) in top-view and at the subsurface (bottom) in a side-view. The white (gray) balls represent surface (subsurface) Pd atoms. The $p(2 \times 2)$ surface unit cells are indicated by black solid lines. b) HAADF-STEM (left) and HR-TEM (right) images of as-synthesized Pd-B$_{40}$ nanoparticles. Scale bars are 50 and 5 nm, respectively. The inset shows the [110] zone axis in a FFT pattern. c) 3D atom maps of Pd-B$_{40}$ fully embedded in a Ni matrix as indicated by the Ni iso-surfaces. Scale bar: 20 nm. d) Extracted region ($2 \times 5 \times 10$ nm$^3$) of interest along the Pd/Ni interface. Yellow, purple, and blue dots mark the reconstructed positions of Ni, Pd, and B atoms, respectively. e) 1D compositional profiles of elements across Pd-B$_{40}$ nanoparticles. The inset image shows a 3D reconstruction of the Pd-B$_{40}$. Scale bar: 20 nm.

**ADVANCED
SCIENCE NEWS**

www.advancedsciencenews.com

**ADVANCED
MATERIALS**

www.advmat.de

Incorporating chemical potentials $\Delta\mu_B$ into the modeling (cf. Figure 1a) allows us to determine which adsorption sites are thermodynamically accessible. For $\Delta\mu_B$ (Pd-B$_{40}$), corresponding to R:P 40 experimental growth conditions, the on-surface adsorption sites become thermodynamically metastable. These sites are at least 1 eV/(B atom) less favorable than subsurface adsorption. If penetration into the subsurface region is kinetically hindered they become the relevant adsorption sites. Using the value at the intersect of the chemical potential and binding energy lines (Figure 1a) we calculate the achievable equilibrium subsurface B concentration as roughly 1.85 B per Pd atom, which is substantially higher than the experimentally determined value. This, together with the observation that the experimental and theoretical concentration of B on the surface roughly agree, suggests that B incorporation into the nanoparticle commences by B atoms binding to the surface being continuously overgrown by subsequent Pd layers, resulting in a homogeneous distribution (Figure S14, Supporting Information).

To further confirm this hypothesis, we immersed a pure Pd wire (99.99+%) into 1.0 M NaBH$_4$ solution (≈100 mole ratio) for 1 h. The following APT analysis of its surface detected only trace amounts of B (<0.001 at%) in the Pd (details in Figures S15 and S16, Supporting Information) indicating that B is indeed integrated during the nanoparticle nucleation/growth process.[31] The B distribution inside the Pd catalyst can hence be controlled by tuning the synthesis conditions, which enables us to control the B-doping level by exploiting the B ingress to our advantage.

The 0.4 M NaBH$_4$ solution results in substantial B-doping of the Pd MNA. Hence, to confirm our expectations, we synthesize two new batches: Pd-B$_1$ (1 mole ratio) and Pd-B$_{0.1}$ (0.1 mole ratio). **Figures 2**a,b show 3D APT atom maps and composition profiles from the analysis of Pd-B$_1$ and Pd-B$_{0.1}$, respectively. The morphology and size are in both cases similar to Pd-B$_{40}$ (Figures S17–S19, Supporting Information). Using X-ray diffraction (XRD), we confirm that all samples are a single phase with a FCC structure (Figures S21 and S22, Supporting Information). Neither boride nor oxide-related phases were found, but the insertion of interstitial B leads to lattice parameter expansion,[27] resulting in an B-concentration related increase of the lattice parameters of B-doped Pd nanoparticles (Figure 2c) compared to the pure-Pd lattice parameter reported to be 0.3890 nm[32] at room temperature.

A lower molar ratio of B during synthesis corresponds to a lower chemical potential of B in solution (cf. Figure 1a), which results in a weakening and destabilization of B binding in on-surface Pd sites with the binding energy for the HCP on-surface site: $E_b$ = −0.57, 0.00, and 0.36 eV/(B atom) for Pd-B$_{40}$, Pd-B$_1$, and Pd-B$_{0.1}$ at 0.25 ML, respectively). In agreement with our expectations of an effectively decreasing B-doping level in the Pd MNA, we find a B content of 2.7, 1.3, and 0.47 at% in Pd-B$_{40}$, Pd-B$_1$, and Pd-B$_{0.1}$, respectively. Note that mole ratio above 1 is commonly reported for synthesizing nanoparticles,[34,35] so regardless of the NaBH$_4$ concentration used during synthesis, most nanoparticles must contain B.

Besides varying the chemical potential, we can also adjust the reaction conditions, since B is progressively integrated during synthesis. Several levers could be used, for example, using *N,N*

dimethylformamide, an organic solvent, and carbon black as a support in an ice-cooled solution; Li et al.[36] achieved 20 at% doping of B in Pd nanoparticles. Here, we simply injected the reducing agent manually drop-by-drop at a relatively slow speed into the solution (≈50 µL s$^{-1}$), allowing more time for B-integration, and achieved 6.7 at% B (Pd-B$_{40s}$). Upon subsequent cooling of the solution to a temperature of 5 °C, we obtained 11.5 at% B (Pd-B$_{40sc}$). In each case, we used the same concentration of reducing agent as for the Pd-B$_{40}$ sample, however, the slower growth rate resulted in 2.5–4.3 times more B being integrated into the Pd-MNA (see details in the Supporting Information). The morphology and size are similar to the other Pd-B samples, and neither B clustering nor surface-segregation is observed (Figures S23 and S24, Supporting Information). Neither batch reached a B saturation in Pd of 18.6 at% as in bulk-Pd at room temperature[33] or 12.7 at% as suggested by the DFT calculations (Figure S20, Supporting Information). The above demonstrates that by precisely controlling the kinetics and chemical potential of B, we can control the B doping level, as schematically summarized in Figure 2d.

The Sabatier principle[37] states that neither too strong nor too weak adsorbate–surface interaction of the reaction intermediate is a key characteristic for a good heterogeneous catalyst.[38] Then, why doping Pd matters? Doping can be exploited to tailor the kinetics, selectivity, and stability of catalyst toward specific reactions.[39,40] As a platinum-group metal, Pd has similar electronic properties to Pt, but its stronger H absorption and adsorption behavior result in slow reaction rates in acidic-HOR.[10] Lattice distortions from the presence of B in bulk Pd[41] change its physical properties and B-doping modifies its catalytic activity.[42,43] Specifically for the alkaline-HOR, the activity originates from a delicate balance of the adsorption strengths of H and OH at the catalyst's surface.[44–46]

To estimate the strength of the chemical bond between the H adsorbate and the (B-doped) metal surface, we use the d-band model.[47] This model assumes that the strength of the bond is determined by the filling of the antibonding states: the higher the d-band center energy (i.e., the closer it is to the Fermi energy), the stronger the chemical bond between adsorbate and substrate. Our analysis of the density-of-states (DOS) and electron density of the considered surfaces (Figure S25, Supporting Information), reveals a downward shift of the d-band center. This is due to an accumulation of electron charge in the vicinity of the subsurface B atoms and results in weaker H-binding on the Pd(111) surface with increasing B coverage.

Hydrogen binding energies, $E_b$(H), calculated for the B-free Pd(111) surface agree with other theoretical[48–51] and experimental[52] reports (see Supporting Information). The H binding energies calculated for varying coverages of H in FCC co-adsorbed with subsurface B, are plotted in **Figure 3**a. For 0, 0.25, and 1 ML B$_{Octa}$ and 1 ML H coverage, we obtain −0.52, −0.37, and 0.32 eV/(H atom), respectively. For reference, we also show in the Figure $E_b$(H) for 0.25 ML H in the FCC site on the pristine Pt(111), that is, −0.46 eV/(H atom).[53] Also shown are the calculated OH binding energies $E_b$(OH) for pristine and for B-doped Pd(111). It has been demonstrated that a weak-binding energy trend from the d-band center model is not always applicable.[54,55] A representative example is the adsorption of adsorbates with an almost full valence shell (such as OH, F,
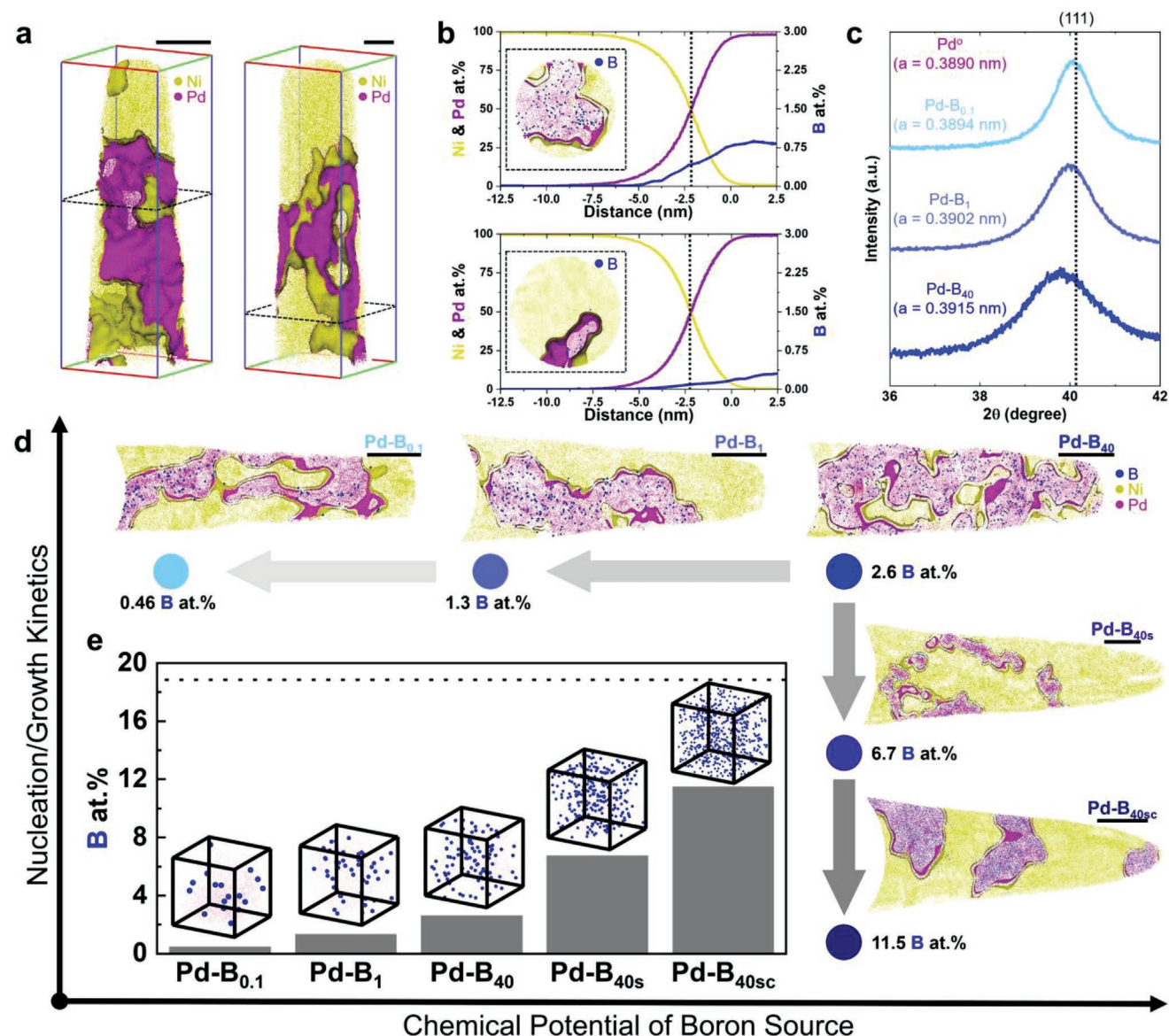
**ADVANCED
SCIENCE NEWS**

www.advancedsciencenews.com

**ADVANCED
MATERIALS**

www.advmat.de

**Figure 2.** Controlling the magnitude of B content in Pd nanoparticles by synthesis. a) 3D atom maps of (left) Pd-$B_1$ and (right) Pd-$B_{0.1}$ nanoparticles embedded in a Ni matrix. b) 1D compositional profile along the Pd/Ni interface for (top) Pd-$B_1$ and (bottom) Pd-$B_{0.1}$. Each inset shows the corresponding top-view tomogram. c) XRD patterns of Pd-$B_x$ samples synthesized with different reductant concentrations. The dotted line represents the (111) peak position. d) Schematic plot of the chemical potential of the boron source versus Pd-$B_x$ nanoparticle growth kinetics. Insets show tomograms (1 nm thin slice along the $x$-axis) of each reconstructed Pd nanoparticle sample. All scale bars are 20 nm. e) B atomic content in Pd-$B_{0.1}$, Pd-$B_1$, Pd-$B_{40}$, Pd-$B_{40s}$, and Pd-$B_{40sc}$ samples. The dotted line represents the maximum B content that FCC Pd metal can absorb without undergoing a phase transformation.[33] The insets show the extracted cuboidal region of interest ($5 \times 5 \times 5$ nm$^3$) of each as-synthesized Pd-$B_x$ nanoparticle.

and Cl) on transition metal surfaces with an almost full d-shell (such as Pd and Pt).[56] For these, we observe a downward shift of the d-band center position for increasing B subsurface doping (cf. Tables S10 and S11, Supporting Information), which strengthens the surface binding energy of OH in contrast to that of H (e.g., $E_b$ [0.5 ML OH at HCP sites] = −2.17, −2.22, and −2.30 eV for 0, 0.25, and 1 ML $B_{Octa}$ co-adsorption, respectively). These results imply that there is an optimal level of doping for which the catalytic activity is boosted due to a weaker interaction of H with the surface at a point where the OH is also not strong.

To verify our hypothesis, we measured linear sweep voltammetry (LSV) of HOR for Pd-$B_{0.1,40,40sc}$ and Pd$_{powder}$ in $H_2$-saturated 0.1 M KOH solution (Figure 3b). The shifts of all catalysts from the reversible H potential (0 $V_{RHE}$) are associated to continuous H absorption.[58] Measured current was normalized with the Pd mass of catalysts. We confirmed that a low level of B-doping improves the activity compared to Pd$_{powder}$, as expected from the decrease in the H surface binding energy, yet at higher doping levels, the activity decreases, which can be attributed to the increased surface binding energy of OH.
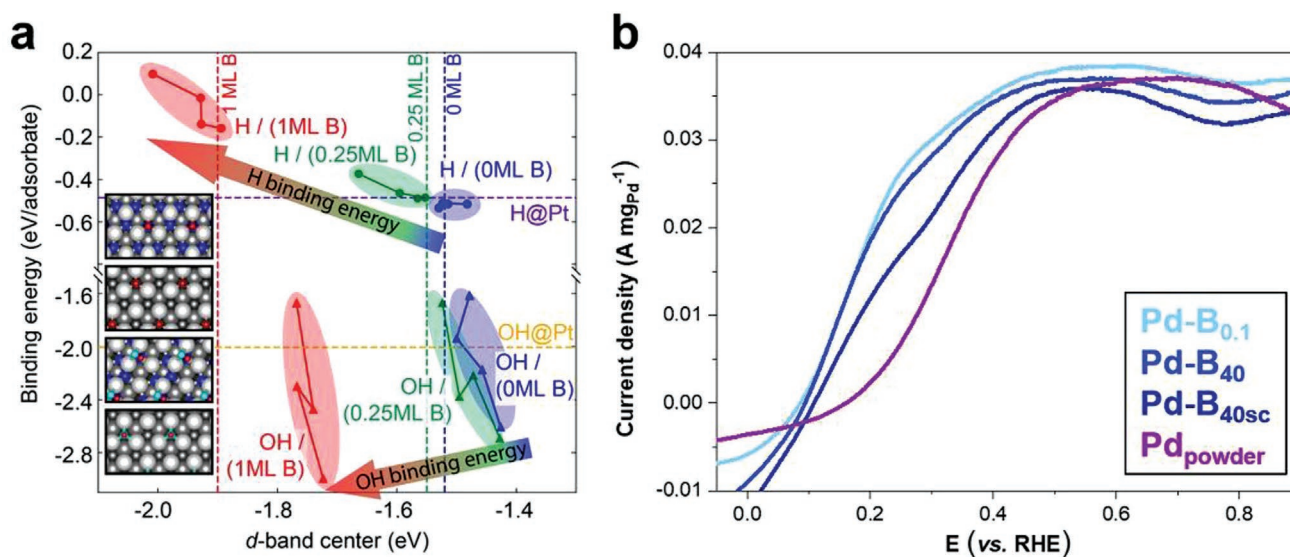
**ADVANCED
SCIENCE NEWS**

www.advancedsciencenews.com

**ADVANCED
MATERIALS**

www.advmat.de

**Figure 3.** HOR binding energy calculations and experiments. a) Calculated H (top part) and OH (bottom part) binding energies plotted as a function of the calculated d-band centers referenced to the Fermi energy. The blue, green, and red lines indicate binding energies for 0.25 to 1 ML H (circle) and OH (triangle) in the presence of 0, 0.25, and 1 ML of $B_{octa}$ in the subsurface of Pd(111), respectively. The horizontal purple and orange dashed lines show the H and OH binding energies for a coverage of 0.25 ML at the most favorable Pt(111) hollow site at the taken from refs. [53, 57]. The vertical dashed lines indicate the calculated d-band centers of only B-doped Pd(111) surfaces. The insets depict H (red) and OH (O: cyan) adsorption on Pd (gray) structures with and without B (blue). b) HOR LSV curve of the as-synthesized Pd-$B_{0.1}$, Pd-$B_{40}$, and Pd-$B_{40sc}$ samples and a reference Pd$_{powder}$. The HOR was performed in a $H_2$-saturated 0.1 M KOH electrolyte with 1600 rpm rotating speed. The LSV curve was measured from 1 to −0.1 V (vs RHE) at a scanning rate of 10 mV s$^{-1}$. The cyclic voltammetry curve and the electrochemical surface area of each Pd catalyst are presented in the Supporting Information.

## 3. Conclusion

We have confirmed a predicted but undesired and uncontrolled incorporation of B arising from the solution during synthesis and proposed, and experimentally confirmed, an approach to design doped metallic nanocatalysts, with a clear influence on their catalytic activity toward the alkaline-HOR. We demonstrated how to engineer concentration of these impurities and control the doping level in the nanoparticles by adjusting the chemical potential and kinetics during synthesis. The presence of subsurface B lowers the binding energy of H on the Pd(111) surface and leads to an increased reaction kinetics at low doping levels, despite the relatively strong increase in the surface binding energy of OH. B-doping hence enables a clear enhancement of the HOR kinetics yet the subtle balance between H and OH binding energies is necessary to design a superior HOR catalyst. Our approach provides a straightforward route to design catalysts that are efficient and stable for the green hydrogen-cycle. Its key idea, tuning impurity ingress from the synthesis solution that can be predicted from ab initio DFT calculations, can be expanded to select impurities based upon their influence on the H- and OH-surface binding energies, but also on their subsurface integration in order to ensure the doping of the catalyst.

## 4. Experimental Section

*Synthesizing Pd Nanoparticles*: 0.01 M of Pd ions solution was prepared by dissolving potassium tetrachloropalladate (99.99%, Sigma-Aldrich) in 5 mL of distilled water. A white sodium borohydride (99.99%, Sigma-Aldrich) powder was dissolved in 5 mL of distilled water according to different mole ratios ([NaBH$_4$]/[K$_2$PdCl$_4$] = 0.1–40).

Then, two solutions were immediately mixed. After bubbles completely stopped, Pd nanoparticles were collected by centrifuging at 5000 rpm for 15 min. Pd nanoparticles were then redispersed in distilled water followed by centrifuging process. Washing process was done for thrice to remove any residuals. The collected Pd nanoparticles were then dried in a vacuum desiccator for 24 h.

*XRD Analysis*: Powder XRD was performed with RIKAKU SmartLab 9kW. The diffraction pattern of as-synthesized Pd samples were measured from the dried nanoparticles powders in 2θ mode using Co Kα radiation ($\lambda$ = 1.54059 Å) and sampling step of 0.01° at scan speed 2° min$^{-1}$.

*XPS Analysis*: XPS measurements were performed by applying a monochromatic Al Kα X-ray source (1486.6 eV) operating at 15 kV and 25 W. C 1s signal at 285.0 eV was used for a reference binding energy scale. The acquired spectra data was then analyzed with the Casa XPS (http://www.casaxps.com/) software.

*TEM Characterization*: HR-TEM and HAADF-STEM were performed using two different Thermo Fisher Titan Themis 60-300 instruments operated at 300 kV, one with an image-corrector and one with a probe-corrector. The chemical composition of each Pd-B$_x$ sample was analyzed by electron energy loss spectroscopy (EELS) and energy-dispersive X-ray spectroscopy (EDS) in the STEM mode. For Pd-B$_{40s}$ and Pd-B$_{40sc}$ samples, TEM and HAADF-STEM analyses were performed inside a JEM-2200FS TEM (JEOL) operating at 200 kV.

*APT Characterization*: The Pd nanoparticle sample was embedded into a Ni matrix using electrodeposition process as shown in Figure S7, Supporting Information. Xe-plasma focused-ion-beam (Thermo Fischer Helios, Eindhoven) was performed to fabricate a needle-shape APT specimen from the codeposited sample following a standard APT specimen preparation.[59] The final APT specimen is shown in Figure S7c, Supporting Information. Needle-shaped specimens were then loaded inside a Cameca LEAP 5000 XS system. APT measurements were performed in pulsed UV laser mode at a detection rate of 1%, a laser pulse energy of 60 pJ, and a pulse frequency of 125 kHz. The specimen temperature was set to 50 K throughout the analysis. Data reconstruction and analyses were performed using the commercial software Imago

visualization and analysis system standard 3.8.4 developed by Cameca Instruments. All 3D atom maps presented here were reconstructed using the standard voltage reconstruction protocol.[60]

*Electrochemical Measurements for HOR in Alkaline*: Electrochemical measurements were performed with a CHI 760e potentiostat at room temperature. Nondoped Pd particles (99.9%, Sigma-Aldrich; <1 µm in size) were used as a reference labeled as $Pd_{powder}$. The catalyst ink was prepared by dispersing 5 mg of the catalyst in 2 ml of isopropyl alcohol and 6.66 µL of Nafion (5 wt% sol. Sigma Aldrich) for 20 min sonication. Subsequently, 7.5 µL of the ink was drop-cast on the glassy carbon disk electrode (surface area = 0.247 cm²). The amount of drop-cast catalyst was appropriate to completely cover the disk electrode. A double junction Hg/HgO filled with 1 M KOH was used as a reference electrode and a carbon rod was used as a counter electrode. Before half-cell tests, a reversible hydrogen electrode (RHE) was calibrate by interconversion point of hydrogen oxidation and evolution current in a high-purity $H_2$-saturated 0.1 M KOH solution using a Pt rotating disk electrode.[61] The as-prepared electrode was inserted into a 100 mL solution of 0.1 M KOH in which Ar gas was purged for 30 min. Cyclic voltammetry was performed at 50 mV s⁻¹ scan rate (0.4–1 V (vs RHE)) three times, then 0.6 V (vs RHE) was applied to the working electrode and $H_2$ gas was bubbled for 30 min. This process was performed to avoid H-adsorption at the open circuit potential. The HOR LSV curve was measured from 1 to −0.1 V (vs RHE) at a scanning rate of 10 mV s⁻¹. The experiment was repeated three times and the results were averaged.

*DFT Calculation*: All presented DFT calculations were performed using the Vienna Ab initio Simulations Package[62,63] with the projector augmented wave approach.[64] The kinetic-energy cutoff employed for the plane-wave basis set was 500 eV. A Γ-centered ($8 \times 8 \times 8$) k-point grid was used for Brillouin-zone integrations for FCC Pd bulk and a ($8 \times 8 \times 1$) grid was used for the Pd(111) $p(1 \times 1)$ surface unit cell as the Pd(111) was the most favorable surface plane for FCC Pd.[65] Equivalently folded k-point meshes were used for larger surface cells. For the exchange-correlation approximation, the generalized gradient approximation due to Perdew, Burke, and Ernzerhof[66] was used. A total of 16 (for Pd) and 3 (for B) electrons were treated as valence, respectively. Electronic and ionic relaxations were carried out until the total energy convergence was less than $10^{-5}$ eV per system, respectively, $10^{-4}$ eV per system. With this setup, the authors obtained a lattice parameter $a = 3.959$ Å and a cohesive energy $E_{coh} = 3.63$ eV for Pd FCC bulk, in good agreement with theoretical[65,67] and experimental[68] results.

For the surface models, a symmetric supercell slab approach was used with an 18 Å vacuum region. Pd(111) slabs were composed of 13 atomic layers and the ensuing slab thickness was 27.44 Å. The three outermost atomic layers were relaxed, while the remaining atoms were fixed to their bulk positions. The calculated surface energy of Pd(111) was 0.091 eV Å⁻², in good agreement with reported theoretical values (0.082 eV Å⁻² by PBE,[69] 0.099 eV Å⁻² by PBEsol[70]) and experiment[71] (0.125 eV Å⁻²).

To account for the various coverages of B, H, and OH on the Pd(111) surface, different sizes of surface unit cells were employed. The coverage (Θ) of each adsorbate atom was defined as the ratio between the number of adsorbate atoms and the number of surface Pd atoms, with an equal number of respective atoms corresponding to 1 ML. For 0.25, 0.5, and 0.75 ML, a $p(2 \times 2)$ surface cell was used and for 1 ML a $p(1 \times 1)$ surface cell was used.

The binding energy ($\Delta E_b$) was calculated as

$$\Delta E_b = \frac{1}{2N_{ads}} \left( E_{tot}^{ads/subs} - E_{tot}^{subs} - 2N_{ads} \cdot \mu_{ads} \right) \tag{1}$$

where $E_{tot}^{ads/subs}$ and $E_{tot}^{subs}$ were the calculated DFT total energies of the adsorbate–substrate and substrate, respectively. $N_{ads}$ was the number of adsorbates in the used surface supercell. $\mu_{ads}$ was the chemical potential of adsorbates with respect to the relevant reference phases at the given experimental condition, defined as

$$\mu_{ads}(c_{ads}, T, pH) = E_{tot}^{ads} + \Delta\mu_{ads}(c_{ads}, T, pH) \tag{2}$$

where $E_{tot}^{ads}$ was the DFT calculated total energy of the adsorbates reference phases (i.e., the $H_2$ molecules for a H adsorbate and the rhombohedral a-phase of boron for a B adsorbate). $\Delta\mu_{ads}$ was the chemical potential difference with respect to its standard reference phase where the source for the adsorbate atom should be an ion in solution. The authors note that $\Delta\mu_H$ should be zero because the $H_2$ gas phase was the relevant reservoir for the considered experiments here, even in the electrochemical measurements. The source of the adsorbed B was a $BH_4^-$ ion in solution, thus $\Delta\mu_B$ was calculated using ref. [72] as follows

$$\Delta\mu_B(c_{BH_4^-}, T, pH) = \mu_{BH_4^-} - 4 \cdot \mu_H - \mu_e \tag{3}$$

where $\mu_{BH_4^-}$, $\mu_H$, and $\mu_e$ were the chemical potentials of $BH_4^-$, H, and the electron, respectively. These could be calculated using tabulated literature data and the experimental conditions (i.e., concentrations of the ions, pH, and temperature) as described in the Supporting Information.

The d-band center was calculated by averaging over the eigen-energy multiplied by the DOS of occupied Pd d-states as specified by the formula:

$$E_{d-center} = \frac{\int_{-\infty}^{E_F} E * DOS(E)}{\int_{-\infty}^{E_F} DOS(E)} \tag{4}$$

where $E$ and $DOS(E)$ were the eigen-energy and the density of Pd d-states, respectively.

## Supporting Information

Supporting Information is available from the Wiley Online Library or from the author.

## Acknowledgements

## Conflict of Interest

The authors declare no conflict of interest.

## Author Contributions

S.-H.K. and S.-H.Y. contributed equally to this work. S.-H.K. and B.G. designed the overall experiment. S.-H.K. performed the synthesis, co-electrodeposition, and atom probe specimen preparation. S.-H.K. measured APT and analyzed the acquired data with support from B.G. J.J. and J.L. performed HR-TEM, (S)TEM-EDS, and EELS measurements with support from C.S. O.K. performed XPS and analyzed data with

[1] T. Pregger, D. Graf, W. Krewitt, C. Sattler, M. Roeb, S. Möller, *Int. J. Hydrogen Energy* **2009**, *34*, 4256.

[2] J. Jia, L. C. Seitz, J. D. Benck, Y. Huo, Y. Chen, J. W. D. Ng, T. Bilir, J. S. Harris, T. F. Jaramillo, *Nat. Commun.* **2016**, *7*, 13237.

[3] A. G. Dutton, J. A. M. Bleijs, H. Dienhart, M. Falchetta, W. Hug, D. Prischich, A. J. Ruddell, *Int. J. Hydrogen Energy* **2000**, *25*, 705.

[4] M. T. Balta, I. Dincer, A. Hepbasli, *Int. J. Hydrogen Energy* **2009**, *34*, 2925.

[5] M. Barakat, B. Tala-Ighil, H. Chaoui, H. Gualous, D. Hissel, *Fuel Cells* **2020**, *20*, 342.

[6] A. E. Lutz, R. S. Larson, J. O. Keller, *Int. J. Hydrogen Energy* **2002**, *27*, 1103.

[7] G. Merle, M. Wessling, K. Nijmeijer, *J. Membr. Sci.* **2011**, *377*, 1.

[8] N. Zhang, Y. Feng, X. Zhu, S. Guo, J. Guo, X. Huang, *Adv. Mater.* **2017**, *29*, 1603774.

[9] N. Zhang, L. Li, Y. Chu, L. Zheng, S. Sun, G. Zhang, H. He, J. Zhao, *Catal. Today* **2019**, *332*, 101.

[10] J. Durst, A. Siebel, C. Simon, F. Hasché, J. Herranz, H. A. Gasteiger, *Energy Environ. Sci.* **2014**, *7*, 2255.

[11] R. K. Singh, E. S. Davydova, J. Douglin, A. O. Godoy, H. Tan, M. Bellini, B. J. Allen, J. Jankovic, H. A. Miller, A. C. Alba-Rubio, D. R. Dekel, *Adv. Funct. Mater.* **2020**, *30*, 2002087.

[12] W. Sheng, H. A. Gasteiger, Y. Shao-Horn, *J. Electrochem. Soc.* **2010**, *157*, B1529.

[13] W. Sheng, M. Myint, J. G. Chen, Y. Yan, *Energy Environ. Sci.* **2013**, *6*, 1509.

[14] J. Lim, S.-H. Kim, R. A. Armengol, O. Kasian, P.-P. Choi, L. T. Stephenson, B. Gault, C. Scheu, *Angew. Chem., Int. Ed.* **2020**, *59*, 5651.

[15] S.-H. Kim, J. Lim, R. Sahu, O. Kasian, L. T. Stephenson, C. Scheu, B. Gault, *Adv. Mater.* **2020**, *32*, 1907235.

[16] K. Jang, S.-H. Kim, H. Jun, C. Jung, J. Yu, S. Lee, P.-P. Choi, *Nat. Commun.* **2021**, *12*, 4301.

[17] J. Johny, O. Prymak, M. Kamp, F. Calvo, S.-H. Kim, A. Tymoczko, A. El-Zoka, C. Rehbock, U. Schürmann, B. Gault, L. Kienle, S. Barcikowski, *Nano Res.* **2022**, *15*, 581.

[18] S.-H. Kim, S.-H. Yoo, P. Chakraborty, J. Jeong, J. Lim, A. A. El-Zoka, X. Zhou, L. T. Stephenson, T. Hickel, J. Neugebauer, C. Scheu, M. Todorova, B. Gault, *J. Am. Chem. Soc.* **2022**, *144*, 987.

[19] R. Du, J. Wang, Y. Wang, R. Hübner, X. Fan, I. Senkovska, Y. Hu, S. Kaskel, A. Eychmüller, *Nat. Commun.* **2020**, *11*, 1590.

[20] N. Hüsing, U. Schubert, *Angew. Chem., Int. Ed.* **1998**, *37*, 22.

[21] H. I. Schlesinger, H. C. Brown, B. Abraham, A. C. Bond, N. Davidson, A. E. Finholt, J. R. Gilbreath, H. Hoekstra, L. Horvitz, E. K. Hyde, J. J. Katz, J. Knight, R. A. Lad, D. L. Mayfield, L. Rapp, D. M. Ritter, A. M. Schwartz, I. Sheft, L. D. Tuck, A. O. Walker, *J. Am. Chem. Soc.* **1953**, *75*, 186.

[22] S. Kidambi, M. L. Bruening, *Chem. Mater.* **2005**, *17*, 301.

[23] T. Maneerung, S. Tokura, R. Rujiravanit, *Carbohydr. Polym.* **2008**, *72*, 43.

[24] Y. Xin, J. Liu, Y. Zhou, W. Liu, J. Gao, Y. Xie, Y. Yin, Z. Zou, *J. Power Sources* **2011**, *196*, 1012.

[25] M. Luty-Błocho, K. Fitzner, V. Hessel, P. Löb, M. Maskos, D. Metzke, K. Pacławski, M. Wojnicki, *Chem. Eng. J.* **2011**, *171*, 279.

[26] K. Kobayashi, K. Kusada, D. Wu, N. Ogiwara, H. Kobayashi, M. Haruta, H. Kurata, S. Hiroi, O. Seo, C. Song, Y. Chen, J. Kim, A. Tayal, O. Sakata, K. Ohara, T. Honma, H. Kitagawa, *Chem. Commun.* **2020**, *56*, 12941.

[27] P. K. Liao, K. E. Spear, M. E. Schlesinger, *J. Phase Equilib.* **1996**, *17*, 340.

[28] S.-H. Kim, P. W. Kang, O. O. Park, J.-B. Seol, J.-P. Ahn, J. Y. Lee, P.-P. Choi, *Ultramicroscopy* **2018**, *190*, 30.

[29] B. Gault, B. Klaes, F. F. Morgado, C. Freysoldt, Y. Li, F. De Geuser, L. T. Stephenson, F. Vurpillot, Microsc. Microanal. **2021**, https://doi.org/10.1017/S1431927621012952.

[30] F. De Geuser, B. Gault, *Acta Mater.* **2020**, *188*, 406.

[31] H. Göksu, *New J. Chem.* **2015**, *39*, 8498.

[32] J. W. Arblaster, *Platinum Met. Rev.* **2012**, *56*, 181.

[33] M. Beck, M. Ellner, E. J. Mittemeijer, *Acta Mater.* **2001**, *49*, 985.

[34] N. R. Jana, L. Gearheart, C. J. Murphy, *Adv. Mater.* **2001**, *13*, 1389.

[35] H. Lee, S. E. Habas, S. Kweskin, D. Butcher, G. A. Somorjai, P. Yang, *Angew. Chem., Int. Ed.* **2006**, *45*, 7824.

[36] J. Li, J. Chen, Q. Wang, W.-B. Cai, S. Chen, *Chem. Mater.* **2017**, *29*, 10060.

[37] P. Sabatier, *La Catalyse En Chimie Organique*, Librairie Polytechnique, Paris, France **1920**.

[38] J. K. Nørskov, T. Bligaard, A. Logadottir, S. Bahn, L. B. Hansen, M. Bollinger, H. Bengaard, B. Hammer, Z. Sljivancanin, M. Mavrikakis, Y. Xu, S. Dahl, C. J. H. Jacobsen, *J. Catal.* **2002**, *209*, 275.

[39] D. Strmcnik, D. Li, P. P. Lopes, D. Tripkovic, K. Kodama, V. R. Stamenkovic, N. M. Markovic, *Top. Catal.* **2015**, *58*, 1174.

[40] A. S. Asundi, A. S. Hoffman, S. S. Nathan, A. Boubnov, S. R. Bare, S. F. Bent, *ChemCatChem* **2020**, *13*, 1186.

[41] K. D. Allard, T. B. Flanagan, E. Wicke, *J. Phys. Chem.* **1970**, *74*, 298.

[42] C. W. A. Chan, A. H. Mahadi, M. M.-J. Li, E. C. Corbos, C. Tang, G. Jones, W. C. H. Kuo, J. Cookson, C. M. Brown, P. T. Bishop, S. C. E. Tsang, *Nat. Commun.* **2014**, *5*, 5787.

[43] T. Thang, V. Doan, J. Wang, K. C. Poon, D. C. L. Tan, B. Khezri, R. D. Webster, H. Su, H. Sato, *Angew. Chem.* **2016**, *55*, 6842.

[44] D. Strmcnik, M. Uchimura, C. Wang, R. Subbaraman, N. Danilovic, D. Van Der Vliet, A. P. Paulikas, V. R. Stamenkovic, N. M. Markovic, *Nat. Chem.* **2013**, *5*, 300.

[45] I. T. McCrum, M. T. M. Koper, *Nat. Energy* **2020**, *5*, 891.

[46] S. Sahoo, D. R. Dekel, R. Maric, S. P. Alpay, *ACS Catal.* **2021**, *11*, 2561.

[47] B. Hammer, J. K. Nørskov, *Nature* **1995**, *376*, 238.

[48] J. F. Paul, P. Sautet, *Phys. Rev. B* **1996**, *53*, 8015.

[49] W. Dong, J. Hafner, *Phys. Rev. B* **1997**, *56*, 15396.

[50] O. M. Løvvik, R. A. Olsen, *Phys. Rev. B* **1998**, *58*, 10890.

[51] S. M. Kozlov, H. A. Aleksandrov, K. M. Neyman, *J. Phys. Chem. C* **2014**, *118*, 15242.

[52] H. Conrad, G. Ertl, E. E. Latta, *Surf. Sci.* **1974**, *41*, 435.

[53] J. R. Kitchin, J. K. Nørskov, M. A. Barteau, J. G. Chen, *Phys. Rev. Lett.* **2004**, *93*, 156801.

[54] J. A. Esterhuizen, B. R. Goldsmith, S. Linic, *Nat. Catal.* **2022**, *5*, 175.

[55] J. A. Esterhuizen, B. R. Goldsmith, S. Linic, *Chem* **2020**, *6*, 3100.

[56] H. Xin, S. Linic, *J. Chem. Phys.* **2010**, *132*, 221101.

[57] A. Michaelides, P. Hu, *J. Chem. Phys.* **2000**, *114*, 513.

[58] S. Henning, J. Herranz, H. A. Gasteiger, *J. Electrochem. Soc.* **2015**, *162*, F178.

[59] K. Thompson, D. Lawrence, D. J. Larson, J. D. Olson, T. F. Kelly, B. Gorman, *Ultramicroscopy* **2007**, *107*, 131.

[60] P. Bas, A. Bostel, B. Deconihout, D. Blavette, *Appl. Surf. Sci.* **1995**, *87–88*, 298.

[61] S. Niu, S. Li, Y. Du, X. Han, P. Xu, *ACS Energy Lett.* **2020**, *5*, 1083.

[62] G. Kresse, J. Furthmüller, *Phys. Rev. B* **1996**, *54*, 11169.

[63] G. Kresse, J. Furthmüller, *Comput. Mater. Sci.* **1996**, *6*, 15.

[64] P. E. Blöchl, *Phys. Rev. B* **1994**, *50*, 17953.

[65] S.-H. Yoo, J.-H. Lee, Y.-K. Jung, A. Soon, *Phys. Rev. B* **2016**, *93*, 35434.

[66] J. P. Perdew, K. Burke, M. Ernzerhof, *Phys. Rev. Lett.* **1997**, *78*, 1396.

[67] G. I. Csonka, J. P. Perdew, A. Ruzsinszky, P. H. T. Philipsen, S. Lebègue, J. Paier, O. A. Vydrov, J. G. Ángyán, *Phys. Rev. B* **2009**, *79*, 155107.

[68] I. Barin, O. Knacke, O. Kubaschewski, *Thermochemical Properties of Inorganic Substances*, Springer-Verlag, Berlin, Germany **1977**.

[69] J. L. F. Da Silva, C. Stampfl, M. Scheffler, *Surf. Sci.* **2006**, *600*, 703.

[70] S.-H. Yoo, J.-H. Lee, B. Delley, A. Soon, *Phys. Chem. Chem. Phys.* **2014**, *16*, 18570.

[71] W. R. Tyson, W. A. Miller, *Surf. Sci.* **1977**, *62*, 267.

[72] M. Todorova, J. Neugebauer, *Phys. Rev. Appl.* **2014**, *1*, 14001.